THE JOURNAL OF
PHYSICAL CHEMISTRY C

Article

Cite This: J. Phys. Chem. C 2018, 122, 5686−5697

pubs.acs.org/JPCC

Mechanistic Insights on Plasmon-Driven Photocatalytic Oxidative Coupling of Thiophenol Derivatives: Evidence for Steady-State Photoactivated Oxygen

Qingfeng Zhang and Hui Wang*

Department of Chemistry and Biochemistry, University of South Carolina, Columbia, South Carolina 29208, United States

Supporting Information

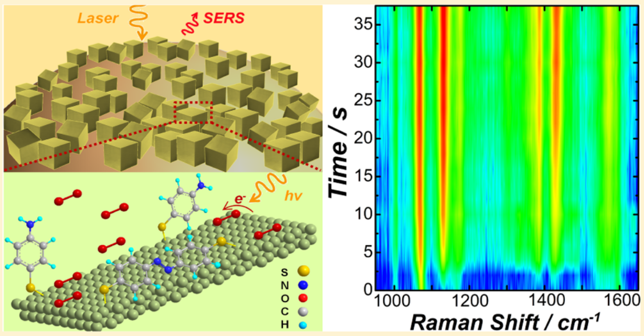

ABSTRACT: The plasmonic electron oscillations in optically excited metallic nanoparticles result in surface confinement of photon energy over much longer time scales in comparison to the unconfined photons traveling at the speed of light, thereby producing an enormous buildup of photon intensity and highly concentrated energetic hot electrons at the nanoparticle surfaces. While the plasmonic hot electrons can be harnessed to drive unconventional photocatalytic molecular transformations at the nanoparticle−molecule interfaces, a set of fundamentally important issues concerning detailed reaction mechanisms still remain poorly understood. Here we use surface-enhanced Raman scattering (SERS) as a unique time-resolving and molecular finger-printing tool to spectroscopically resolve the complex kinetics and underlying pathways of plasmon-driven oxidative coupling of thiophenol derivatives chemisorbed on the surfaces of optically excited plasmonic Ag nanostructures. A hybrid suprananostructure composed of an SiO_2 bead densely decorated with Ag nanocubes was used as both the SERS substrate and the plasmonic photocatalyst under near-infrared excitations. Through deliberately designed time-resolved single-particle SERS measurements, we have been able to pinpoint the effects of excitation power, local-field enhancement, interfacial oxygen abundance, molecular structures, and photothermal heating on the kinetics and yields of the hot electron-driven oxidative coupling reactions. Our time-resolved SERS results provide compelling experimental evidence for the steady-state photoactivated oxygen, revealing that the chemical transformations of thiophenol derivatives rather than the photo-activation of interfacial oxygen constitute the kinetic bottlenecks along the multistep reaction pathways, while the overall reaction rates are dynamically maneuvered by the photoactivated oxygen at its steady-state concentrations.

INTRODUCTION

Optically excited plasmonic nanoparticles can catalyze a unique set of interfacial molecular transformations boosted by the enormous buildup of photon intensity[1−4] and high abundance of energetic ballistic electrons, also known as hot electrons,[5−10] at the nanoparticle surfaces. Because of a lack of coherence, the plasmonic hot carriers are fundamentally different from the excitons in semiconductors, making it possible to drive photochemical reactions along unconventional pathways distinct from those involved in conventional thermal catalytic reactions and semiconductor-based photocatalysis.[10−16] It has been demonstrated that plasmonic hot electrons can be efficiently harnessed to drive or enhance intriguing photocatalytic reactions, such as light-induced nanocrystal growth,[16−20] photopolymerization,[21,22] dissociation of H_2,[23,24] water splitting,[12,25] nitrothiophenol reduction,[26−29] selective oxidation,[11,14,30−34] and the Suzuki coupling reactions.[35−37] While the generation and migration of hot electrons upon plasmonic excitation and decay are fast photophysical processes over time scales from femtoseconds to picoseconds,[8,10,15,31] the plasmon-driven photocatalytic reactions typically occur on drastically longer time scales ranging from a few seconds up to several hours,[11,13,22−24,30,31,33] strongly indicating that slow interfacial chemical or photochemical processes, most likely the photo-activation of crucial interfacial species or induced transformations of molecular adsorbates, constitute the kinetic bottlenecks along the multistep reaction pathways. It still remains an immensely challenging task, however, to fully elucidate the detailed reaction mechanisms, largely because of the intrinsic complexity of multiple intriguing photophysical, photochemical, and interfacial processes entangled in the plasmon-driven photocatalytic molecular transformations.

A key step in plasmon-driven photocatalysis has been identified to be the photo-activation of crucial species upon injection of plasmonic hot electrons into the unpopulated orbitals of the molecular adsorbates, which selectively activates certain types of chemical bonds and creates highly reactive transient species that dynamically modulate the interfacial molecular transformations.[10,13,31] This is best manifested by the photo-activation of triplet oxygen, $^3O_2$, adsorbed on plasmonic

Received: January 19, 2018
Revised: February 17, 2018
Published: February 20, 2018

DOI: 10.1021/acs.jpcc.8b00660
J. Phys. Chem. C 2018, 122, 5686−5697

nanoparticle surfaces, which generates transient doublet $^2O_2^-$, a highly active oxidative species that selectively drives a series of aerobic oxidation reactions, such as epoxidation of ethylene,[11,14,30,34] oxidation of CO,[30] and oxidative coupling of aminothiophenol.[38] Although multiple experimental evidences have coherently verified the existence of such photoactivated oxygen,[13,30,34,38] what the rate-limiting steps are and how the transient photoactivated oxygen dynamically modulates the reaction kinetics still remain fundamentally intriguing open questions, inspiring us to perform detailed kinetic studies to fully understand the dynamic nature of the photoactivated oxygen and pinpoint the underlying rate-determining factors using plasmon-driven photocatalytic oxidative coupling of thiophenol derivatives as prototypical model reactions.

The formation of 4,4′-dimercaptoazobenzene (DMAB) through photocatalytic oxidative coupling of 4-aminothiophenol (4-ATP) adsorbed on optically exited plasmonic nanoparticles represents an enthralling plasmon-driven paradigm for unconventional synthesis of aromatic azo compounds.[28,32,33,38] This photocatalytic reaction was first discovered in 2010 when several Raman peaks signifying the characteristic a_g modes of DMAB emerged in the surface-enhanced Raman scattering (SERS) spectra upon laser illumination of 4-ATP chemisorbed on metallic nanostructures.[32,33] These characteristic SERS peaks of DMAB, first observed by Osawa and co-workers back in 1994,[39] had long been controversially interpreted as the b_2 modes of 4-ATP enhanced by interfacial charge transfers until Tian and co-workers convincingly proved that 4-ATP underwent an oxidative coupling process with the aid of photoactivated oxygen to form DMAB during SERS measurements.[33,38] Although this plasmon-driven coupling reaction has been intensively investigated using a large variety of plasmonic nanostructures as the photocatalysts under a diverse range of reaction conditions,[28,32,33,38,40−42] several key aspects regarding the detailed mechanisms still remain unclear. (1) The rate-limiting step needs to be identified, based on which the derivation of an empirical rate law becomes possible. (2) It still remains an open question whether the overall reaction kinetics is dynamically tied to the interfacial abundance of the photoactivated oxygen. (3) The search for optimal plasmonic photocatalysts has been conducted in a largely empirical fashion because of a lack of quantitative understanding of the detailed correlations between plasmonic field intensity and reaction kinetics. (4) The plasmonic photothermal heating may thermally activate the molecular adsorbates on the nanoparticle surfaces and thereby alter the activation energy barriers of interfacial reactions. How the photothermal heating influences the reaction kinetics and yields is well-worthy of further scrutiny. (5) Substitution of the hydrogen atoms in the amine group of 4-ATP with other functional groups may significantly modify the reaction energy landscapes. However, such molecular structural effects still remain unexplored. To shed light on these fundamentally intriguing but intrinsically complex issues, we use SERS as a time-resolving and molecular finger-printing tool to fully resolve the complex kinetics of oxidative coupling of several thiophenol derivatives chemisorbed on plasmonic photocatalysts. Time-resolved SERS provides a unique means to quantitatively correlate the reaction kinetics with the plasmonic characteristics of the photocatalysts, enabling us to pinpoint the effects of several key factors dictating the reaction kinetics and yields, such as excitation laser power, local-field enhancement, abundance of interfacial oxygen, molecular structures of thiophenol derivatives, and plasmonic photothermal annealing. As revealed by this work, the rate-limiting step is essentially associated with the interfacial chemical transformations of the thiophenol derivatives, while the overall reaction kinetics is dynamically maneuvered by the photoactivated oxygen at its steady-state concentrations.

■ METHODS

Core-satellite suprananoparticles (SNPs), each of which was composed of a spherical SiO_2 core densely decorated with Ag nanocubes (NCs), were used as both the SERS substrates and the plasmonic photocatalysts. The SiO_2@Ag NC SNPs were assembled by electrostatically attaching the Ag NCs onto the surfaces of polydiallyl-dimethylammonium (PDDA)-functionalized SiO_2 beads through a layer-by-layer assembly process[43] (see details in the Supporting Information). The structures, compositions, and surface properties of the as-assembled SNPs were characterized by transmission electron microscopy (TEM), scanning electron microscopy (SEM), energy-dispersive spectroscopy (EDS), optical extinction spectroscopy, and ζ-potential measurements (see details in the Supporting Information). Submonolayers of isolated SiO_2@Ag NC SNPs were immobilized onto poly(4-vinylpyridine)-functionalized silicon substrates following a previously reported protocol[44] (see details in the Supporting Information). To form self-assembled monolayers of the thiophenol derivatives on the nanoparticle surfaces, the SiO_2@Ag NC SNPs immobilized on silicon substrates were incubated with 500 μM 4-ATP, 4-dimethylamino-thiophenol (4-DMATP), or 4-acetamido-thiophenol (4-AATP) ethanolic solution at room temperature for 24 h, thoroughly washed with ethanol and water, and then finally dried with N_2 gas.

Time-resolved SERS spectra were collected using a BaySpec Nomadic Raman microscope built on an Olympus BX51 reflected optical system under 785 nm laser excitation in the confocal mode (focal area of 2 μm diameter). A 50× dark field objective (NA = 0.5, WD = 10.6 mm, Olympus LMPLFLN-BD) was used for both Raman signal collection and dark field scattering imaging. The laser beam was focused on individual SiO_2@Ag NC SNPs for Raman spectrum collection. The spectral acquisition time was typically 2 s, unless mentioned otherwise, and the power of the excitation laser focused on the samples was adjusted using a neutral density filter and measured using a laser power meter (Newport, model: PMKIT-05-01). The photocatalytic reactions were carried out in various atmospheres, such as ambient air, pure oxygen, pure nitrogen, and oxygen/nitrogen mixtures at 1 atmospheric pressure and room temperature. Under each experimental condition, the kinetic measurements were repeated on 10 different SiO_2@Ag NC SNPs, one particle at a time. Normal Raman spectra were collected on solid thin films of 4-ATP, 4-DMATP, and 4-AATP on silicon substrates.

■ RESULTS AND DISCUSSION

Our SERS-based kinetic studies involved the use of deliberately designed, bifunctional SiO_2@Ag NC SNPs as both the SERS substrate and the plasmonic photocatalyst. Monodisperse Ag NCs with edge lengths of 35.9 ± 1.62 nm were synthesized following a protocol developed by Xia and co-workers,[45] and carboxylate-functionalized spherical SiO_2 beads with uniform diameters of 1.00 ± 0.0240 μm were purchased from Bangs Laboratories, Inc. (Figure S1 in the Supporting Information). When dispersed in water at neutral pH, colloidal SiO_2 beads

DOI: 10.1021/acs.jpcc.8b00660
J. Phys. Chem. C 2018, 122, 5686−5697

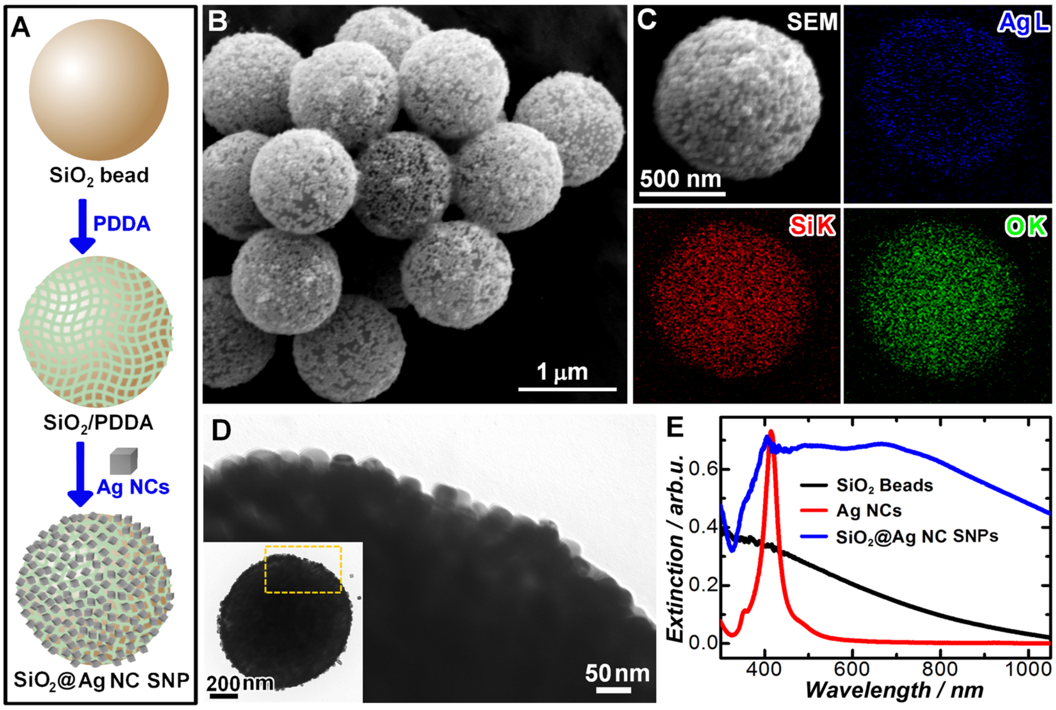

Figure 1. Assembly of SiO_2@Ag NC SNPs. (A) Schematic illustration of the assembly of SiO_2@Ag NC SNPs. (B) SEM image of SiO_2@Ag NC SNPs. (C) SEM image and EDS elemental distribution maps (based on the intensities of Ag-L, Si-K, and O-K lines) of SiO_2@Ag NC SNPs. (D) TEM image of an SiO_2@Ag NC SNP. The inset shows the TEM image of the entire particle and the region enclosed by the dash box is shown with a higher magnification. (E) Optical extinction spectra of colloidal SiO_2 beads, Ag NCs, and SiO_2@Ag NC SNPs.

and Ag NCs were both negatively charged on their surfaces. We used a thin layer of positively charged polymer, PDDA, as the linker between the SiO_2 bead and the Ag NCs to construct SiO_2@Ag NC SNPs through an electrostatic layer-by-layer assembly approach[43] (Figure 1A). The evolution of the surface charges of the particles during the stepwise assembly process was monitored by ζ-potential measurements (Figure S2 in the Supporting Information). The surface of each SiO_2 bead was densely decorated with Ag NCs, as clearly shown by the electron microscopy images (Figure 1B—D) and EDS-based elemental analysis (Figures 1C and S3 in the Supporting Information). While colloidal Ag NCs exhibited a narrow plasmon resonance band centered at 415 nm, the SiO_2@Ag NC SNPs displayed a broad spectral feature in the optical extinction spectrum with plasmon resonance red-shifted into the near-infrared (Figure 1E) because of strong plasmon coupling between adjacent Ag NCs,[46] allowing us to excite the plasmons over a broad spectral range across the visible and near-infrared regions to achieve large SERS enhancements as well as high photocatalytic efficiency. In this work, we used a continuous wave 785 nm laser as the excitation source for both SERS and photocatalysis. The SiO_2 beads did not exhibit any plasmonic spectral features in the visible and near-infrared regions, thereby serving solely as a dielectric substrate supporting the Ag NCs. The plasmonic "hot-spots" located inside the sub-10 nm gaps between neighboring Ag NCs provided enormous field enhancements exploitable not only for enhancing Raman signals but for producing high surface abundance of hot electrons as well. The as-assembled SiO_2@Ag NC SNPs could be immobilized onto poly(4-vinylpyridine)-functionalized silicon substrates[44,47] to form a submonolayer of well-separated individual particles (Figure S4 in the Supporting Information). Thiophenol derivatives, such as 4-ATP, 4-DMATP, and 4-AATP, strongly adsorbed onto the Ag NC surfaces through covalent Ag—S interactions to form self-assembled monolayers while well-preserving the structural integrity of the SNPs without causing observable detachment of Ag NCs from the silica cores (Figure S5 in the Supporting Information). We used a confocal Raman microscope/spectrometer to focus the excitation laser onto 2 μm × 2 μm regions containing individual SiO_2@Ag NC SNPs, which allowed us to resolve the photocatalytic reaction kinetics on one SNP at a time through time-resolved SERS measurements.

Plasmon-driven photocatalytic reactions are initiated by the optical excitation of collective oscillations of valence electrons, also known as plasmons, in the photocatalysts. Following the optical excitation, the plasmonic electron oscillations can dephase through either radiative elastic photon scattering or nonradiative relaxation pathways, namely, Landau damping (generation of hot electrons and holes in the metals) or chemical interface damping (direct electron injection into the molecular adsorbates on the nanoparticle surfaces).[31] The radiative decay of plasmons gives rise to tremendously enhanced local electromagnetic fields exploitable for SERS, while the nonradiative plasmon decay involves charge transfers between strongly coupled nanoparticles and molecular adsorbates, triggering photochemical transformations on the surfaces of plasmonic nanostructures.[13] As illustrated in Figure 2A, the plasmonic excitation of an Ag nanoparticle creates a nonthermal distribution of energetic hot electrons transiently occupying the empty states above the Fermi level while leaving the hot holes below the Fermi level of Ag (−4.3 eV vs vacuum). The transfer of hot electrons from Ag to molecular adsorbates becomes possible when energetically favorable band alignments exist between the excited hot electrons and the unoccupied adsorbate states. Upon plasmonic excitation at 785 nm (photon

DOI: 10.1021/acs.jpcc.8b00660
J. Phys. Chem. C 2018, 122, 5686−5697

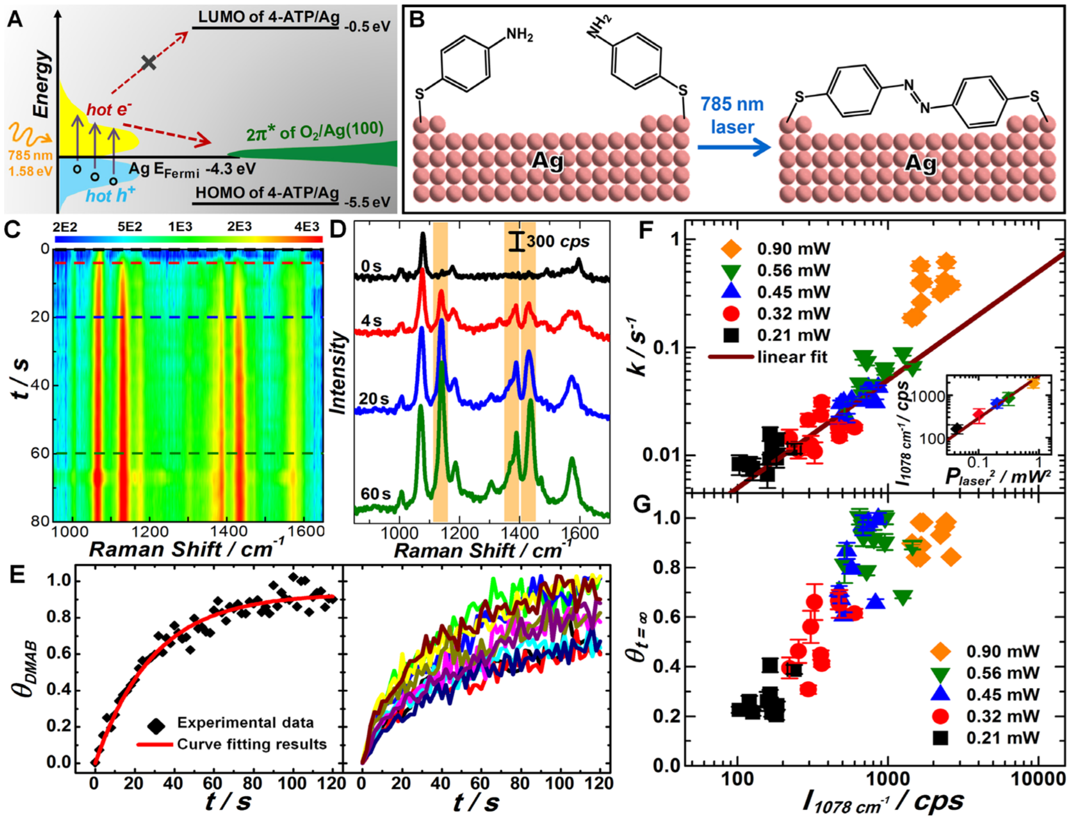

Figure 2. Kinetics of plasmon-driven oxidative coupling of 4-ATP. (A) Schematic illustration of plasmonic hot electron-driven photo-activation of O_2 adsorbed on Ag surfaces. All the orbital energies are defined using the vacuum as the reference state at 0 eV. (B) Schematic illustration of plasmon-driven dimerization of 4-ATP chemisorbed on Ag NC surfaces under 785 nm laser excitation. (C) Time-resolved SERS spectra collected on one 4-ATP-coated SiO_2@Ag NC SNP upon exposure to 785 nm laser illumination under ambient conditions. The spectral acquisition time was 2 s, and the laser power was 0.45 mW. (D) Snapshot SERS spectra collected at reaction times of 0, 4, 20, and 60 s. The highlighted 1440, 1390, and 1140 cm^{-1} bands are spectral signatures of DMAB. (E) Temporal evolution of θ_{DMAB} obtained from the time-resolved SERS results shown in panel C on one SiO_2@Ag NC SNP (left panel) and θ_{DMAB} trajectories collected on 10 different SiO_2@Ag NC SNPs under identical experimental conditions (right panel). The least-squares curve fitting results are shown as a solid curve in the left panel. Plots of (F) k and (G) $\theta_{t=\infty}$ vs $I_{1078cm^{-1}}$ collected on individual SiO_2@Ag NC SNPs at excitation powers of 0.21, 0.32, 0.45, 0.56, and 0.90 mW. The time-resolved SERS measurements were performed on 10 different SiO_2@Ag NC SNPs at each excitation power, and the error bars represent the standard deviations of least-squares curve fitting. The inset of panel (F) shows the plots of the ensemble averaged $I_{1078cm^{-1}}$ as a function of laser power square, P_{laser}^2.

energy of 1.58 eV), the hot electrons were distributed in an energy range insufficient for them to be injected into the lowest unoccupied molecular orbital of 4-ATP chemisorbed on Ag (3.8 eV above the Ag Fermi level).[48,49] However, previous density functional theory (DFT) calculations showed that the energy of the antibonding $2\pi^*$ orbitals of molecular $^3O_2$ adsorbed on the Ag {100} facet (the dominant facet on the surfaces of Ag NCs[45]) matched the Ag Fermi level very well,[30] thereby facilitating the transfer of a hot electron from Ag to the $2\pi^*$ orbitals of $^3O_2$ adsorbate to form $^2O_2^-$, a short-lived, photoactivated species that may either rapidly react with other molecular adsorbates, as exemplified by the oxidative coupling of thiophenol derivatives studied in this work, or relax to its ground electronic state after the decay of an electron in the antibonding $2\pi^*$ orbitals back to Ag. Immediately after the photoactivated $^2O_2^-$ reacted with chemisorbed 4-ATP to initiate the coupling reaction, an electron might rapidly recombine with a hole in the plasmonically excited Ag NC, preventing the Ag NC from being oxidized. After the photocatalytic oxidative coupling reactions, the morphology of Ag NCs and the distribution of Ag NCs on the SiO_2 core were both well-preserved (Figure S6 in the Supporting Information), indicating that the laser illumination and the photocatalytic reactions did not cause any oxidation or dissolution of the Ag NCs observable within the resolution of SEM. The possibility of forming transient, locally oxide Ag surfaces during the photocatalytic reactions, however, had not been ruled out simply based on the ex situ SEM imaging results.

While neither the ground-state nor the photo-excited interfacial oxygen was spectroscopically resolvable by SERS, the formation of the product, DMAB, could be monitored in real time based on the temporal evolution of the characteristic SERS peaks of DMAB. Although this photocatalytic reaction involved multiple steps, many of which were indecipherable by SERS, a simplified version depicted as the dimerization of 4-ATP to form DMAB on the Ag surface (Figure 2B) fully captured the essential SERS-resolvable chemical transformation. Figure 2C,D shows the temporal evolution of SERS spectra of 4-ATP adsorbed on SiO_2@Ag NC SNPs upon exposure to the continuous wave excitation laser (wavelength: 785 nm; power: 0.45 mW; focal plane: 3.14×10^{-8} cm^2; power density: 14 kW cm^{-2}) under the ambient aerobic condition at room temperature. Prior to the formation of DMAB, the two major SERS peaks at 1078 and 1595 cm^{-1} were assigned to the C−S stretching mode and the benzene ring mode of 4-ATP.[32,33] As the photocatalytic reaction proceeded, several newly emerged peaks at 1140, 1390, and 1440 cm^{-1} gradually became more intense, signifying the formation of DMAB.[33,38] Meanwhile, the benzene ring mode downshifted from 1595 to 1575 cm^{-1}, whereas the C−S stretching mode slightly downshifted by 4 cm^{-1} upon the formation of DMAB. The transformation of 4-ATP into DMAB also resulted in significantly stronger SERS signals because DMAB had much larger Raman cross-sections than those of 4-ATP.[33,38] The detailed peak assignments were listed in Tables S1 and S2 in the Supporting Information.

We quantified the temporal evolution of the apparent fraction of DMAB, θ_{DMAB}, based on the relative peak intensities of the 1440 cm^{-1} Raman mode (N=N stretching mode of DMAB) with respect to the C−S stretching modes of the molecules around 1078 cm^{-1} (see details in the Supporting Information). In the left panel of Figure 2E, we plotted the temporal evolution of θ_{DMAB} on one SiO_2@Ag NC SNP, which exhibited a typical first-order kinetic curve. The apparent first-order rate constant, k, and the maximum reaction yield at the infinitely long reaction time, $\theta_{t=\infty}$, were obtained by performing least-squares curve fitting to the θ_{DMAB} trajectory with the following first-order rate equation

$$\theta_{DMAB} = \theta_{t=\infty} \times (1 - e^{-k\times t}) \tag{1}$$

We repeated the time-resolved SERS measurements on 10 different SiO_2@Ag NC SNPs one particle at a time under exactly the same reaction conditions, and all the θ_{DMAB} trajectories are shown in the right panel of Figure 2E. Although both k and $\theta_{t=\infty}$ varied from particle to particle because of the intrinsic structural heterogeneity and the variation of average field enhancements among the SNPs, all the θ_{DMAB} trajectories could be well-fitted with the first-order rate law. The photocatalytic coupling of 4-ATP is mechanistically complex, involving the plasmonic excitation of the SNPs, photoactivation of interfacial oxygen, and multistep chemical transformations cascaded by multiple intermediates along the reaction pathways. However, the kinetics of DMAB formation obeyed a surprisingly simple first-order rate law, strongly indicating that the overall reaction kinetics was determined by one kinetically sluggish rate-limiting step associated with the formation of a transient intermediate species that rapidly transformed into other short-lived intermediates or the final product, DMAB. The first-order kinetics observed here could be most reasonably interpreted as a consequence of molecular transformations driven by photoactivated oxygen at its steady-state concentrations, which could be described by two key rate-determining steps shown below.

$$\text{Step 1: } O_2^{ad} \underset{-e^-\cdot k_{-1}}{\overset{+\text{hot } e^-\cdot k_1}{\rightleftharpoons}} O_2^-$$

$$\text{Step 2: } O_2^- + \text{4-ATP} \xrightarrow{k_2} \text{TI*} \xrightarrow{\text{fast}} 1/2\text{DMAB}$$

The photoactivation of interfacial oxygen involved the injection of energetic hot electrons from Ag to surface-adsorbed O_2, which is denoted as O_2^{ad}, following the plasmonic excitation. k_1 is the rate constant for the photoactivation, while k_{-1} is the rate constant defining the kinetics of the reverse reaction, the thermal relaxation of the photoactivated oxygen back to its ground state. In the context of the proposed steady-state kinetics, both the photoactivation and thermal deactivation of interfacial oxygen (step 1) were considered to be much faster than the rate-limiting step (step 2), rapidly reaching an equilibrium that kept the photoactivated oxygen at its steady-state concentration. The photoactivated oxygen subsequently reacted with the surface-adsorbed 4-ATP to initiate the stepwise oxidative dehydrogenation and azo-coupling reactions to eventually form DMAB. While the transient intermediates were unidentifiable by time-resolved SERS, possibly because of their short life times, the rates of DMAB formation were essentially determined by the rate-limiting step with a rate constant of k_2, which was most likely associated with the formation of a partially dehydrogenated transient intermediate, denoted as TI*. All the other faster steps along the reaction pathways, however, could be ignored in this simplified two-step mechanism, based on which we were able to derive the rate law describing the formation kinetics of DMAB.

The formation rates of the photoactivated oxygen and DMAB could be described by eqs 2 and 3, respectively, where all the concentration terms referred to the interfacial abundance of the species adsorbed on photocatalyst surfaces.

$$\frac{d[O_2^-]}{dt} = k_1[O_2^{ad}] - k_{-1}[O_2^-] - k_2[O_2^-][\text{4-ATP}] \tag{2}$$

$$\frac{d[\text{DMAB}]}{dt} = k_2[O_2^-][\text{4-ATP}] \tag{3}$$

When the photoactivated oxygen reached its steady-state concentration, $[O_2^-]_{ss}$

$$\begin{aligned}\frac{d[O_2^-]_{ss}}{dt} &= k_1[O_2^{ad}] - k_{-1}[O_2^-]_{ss} - k_2[O_2^-]_{ss}[\text{4-ATP}] \\ &= 0\end{aligned} \tag{4}$$

Rearrangement of the terms in eq 4 led to the following expression

$$[O_2^-]_{ss} = \frac{k_1[O_2^{ad}]}{k_{-1} + k_2[\text{4-ATP}]} \tag{5}$$

Considering that the values of both k_1 and k_{-1} were far greater than that of k_2, eq 5 could be further simplified as

$$[O_2^-]_{ss} \approx \frac{k_1}{k_{-1}}[O_2^{ad}] \tag{6}$$

The rate of DMAB formation in the presence of steady-state O_2^- could be expressed as

$$\frac{d[\text{DMAB}]}{dt} = k_2[O_2^-]_{ss}[\text{4-ATP}] \tag{7}$$

Therefore, the apparent first-order rate constant, k, obtained from the experimentally resolved kinetic data was related to both k_2 and $[O_2^-]_{ss}$, as described by the following equation

$$k = k_2[O_2^-]_{ss} \tag{8}$$

Combining eqs 6 and 8 resulted in the following expression for k

$$k = k_2\frac{k_1}{k_{-1}}[O_2^{ad}] \tag{9}$$

Equation 9 related the experimentally measured k to k_1, k_{-1}, k_2, as well as the interfacial abundance of surface-adsorbed $^3O_2$, $[O_2^{ad}]$, providing a central guiding principle for us to rationally maneuver the rate of DMAB formation by varying the reaction conditions. While k_{-1} was intrinsically tied to the nature of molecular oxygen and Ag surfaces, k_1 could be experimentally modulated by either adjusting the excitation laser power or varying the field enhancements of the plasmonic photocatalysts. The rate of DMAB could also be modulated by varying the partial pressure of O_2 in the reaction atmosphere, which controlled $[O_2^{ad}]$ on the photocatalyst surfaces. In contrast, k_2 was unrelated to the photoactivation of interfacial oxygen but varied with the molecular structures of the thiophenol derivatives as well as the photothermal annealing of the surface adsorbates on the plasmonic photocatalysts. Here, we demonstrated that k_1, k_2, and $[O_2^{ad}]$ could all be systematically tuned to finely maneuver the reaction kinetics by deliberately tailoring several key experimental parameters, through which compelling experimental evidences could be obtained to further verify the proposed steady-state kinetic model.

We first demonstrated that the rate of DMAB formation could be maneuvered by modulating k_1 through variation of the excitation power while keeping all the other experimental parameters unchanged. We measured the kinetics of DMAB formation on one SiO_2@Ag NC SNP each time at 5 different excitation powers of 0.21, 0.32, 0.45, 0.56, and 0.90 mW. At each excitation power, the single-particle SERS-based kinetic measurements were performed on 10 individual SNPs. On a given SNP photocatalyst with field enhancement of $|E|/|E_0|$, the amplitude of the enhanced plasmonic fields, $|E|$, was directly proportional to the electric field intensity of the incident laser, $|E_0|$. As shown in the inset of Figure 2F, the SERS intensity of 4-ATP at 1078 cm^{-1} prior to the photoreactions, $I_{1078cm^{-1}}$, was proportional to the square of the excitation power, P_{laser}^2 ($P_{laser} \propto |E_0|^2$), further verifying the $|E|^4$-dependence of SERS signals when the Raman enhancements were dominated by the electromagnetic mechanism.[4,50−52] Increasing the excitation power led to faster generation of hot electrons and higher magnitudes of local fields, both of which were highly desired for boosting the photoactivation of interfacial oxygen, resulting in higher k_1 values without changing k_{-1}. As a consequence, the equilibrium between photoactivation and thermal deactivation of interfacial oxygen was shifted toward the photoactivated state at higher excitation powers, increasing the steady-state concentration of the photoactivated oxygen and thus the rate of DMAB formation (Figure 2F).

The single-particle SERS results further enabled us to quantitatively correlate the reaction rates with the local fields on the surfaces of the photocatalysts. While both k and $I_{1078cm^{-1}}$ varied form particle to particle even at the same excitation power because of the structural heterogeneity among the SiO_2@Ag NC SNPs, a general trend that k increased with $I_{1078cm^{-1}}$ could be clearly observed (Figure 2F). At excitation power below 0.56 mW, k was found to be proportional to $I_{1078cm^{-1}}$. Because $I_{1078cm^{-1}}$ scaled with the fourth power of average field intensity, $|E|^4$, k was also proportional to $|E|^4$. The $|E|^4$ dependence of k that we observed suggested that the hot electron transfer from Ag to the $2\pi^*$ orbitals of surface-adsorbed $^3O_2$ was most likely mediated by Landau damping rather than chemical interface damping. While the rate of direct hot electron transfer during chemical interface damping is proportional to the transition dipole moment, which scales with $|E|^2$, Landau damping involves two key steps, the excitations of hot electrons and holes in the metal and the subsequent transfer of hot electrons from the metal to the molecular adsorbates. The rates of both steps are proportional to $|E|^2$, giving rise to the overall $|E|^4$ dependence. As previously calculated by the DFT, the oscillator strengths of plasmon excitations were much larger than that those of the direct charge transfer transitions between Ag and surface-adsorbed oxygen.[48] Both our experimental observations and previous DFT calculations coherently indicated that the hot electron transfer through Landau damping was the major charge transfer channel for the photoactivation of oxygen on the surfaces of the Ag photocatalysts under near-infrared excitations. Although its quantum efficiency of hot electron transfer is typically much lower than that of chemical interface damping,[6,13,31] Landau damping provides more room for us to boost the photocatalytic reactions by optimizing the near-field plasmonic properties of the photocatalysts because the rates of photocatalytic reactions mediated by Landau damping are more sensitively dependent on the local fields ($|E|^4$ for Landau damping vs $|E|^2$ for chemical interface damping). Whether such $|E|^4$ versus $|E|^2$ dependence of k can be used as a universal criterion to distinguish Landau damping from chemical interface damping still needs to be further tested in other plasmon-driven photocatalytic reaction systems. In this work, we excited the plasmon resonance at 785 nm to ensure that the interfacial oxygen was photoactivated upon the transfer of a plasmonic hot electron from Ag to the $2\pi^*$ orbitals of surface-adsorbed $^3O_2$. Increasing the photon energy of the excitation laser allows the hot electrons to be excited to higher energies with respect to the Ag Fermi level with drastically modified energy distribution profiles, making it possible to switch the dominant hot electron decay pathways from Landau damping to chemical interface damping and even to inject the hot electrons into other unoccupied orbitals of the molecular adsorbates. Detailed investigations of the effects of the excitation wavelength on the reaction kinetics and mechanisms are currently underway.

As shown in Figure 2F, k exhibited a linear dependence on $I_{1078cm^{-1}}$ in the low excitation regime below 0.56 mW but started to show a superlinear power-law dependence on $I_{1078cm^{-1}}$ as the excitation powder was further increased to 0.90 mW. We hypothesized that at relatively low excitation powers, the photothermal effect was insignificant. However, above a certain threshold excitation power, the photothermal heating of the surface-adsorbed thiophenol derivatives became an additional dominant factor that further speeded up the reactions. Another noteworthy observation was that $\theta_{t=\infty}$ also increased with $I_{1078cm^{-1}}$; in other words, $\theta_{t=\infty}$ increased with $|E|$ on the photocatalysts. At relatively high excitation power above 0.56 mW, the reactions proceeded to $\theta_{t=\infty}$ very close to 1 on most SiO_2@Ag NC SNPs, whereas at lower excitation powers, the majority of SiO_2@Ag NC SNPs exhibited $\theta_{t=\infty}$ significantly lower than 1 (Figure 2G). At first glance, the observed relationship between $\theta_{t=\infty}$ and $|E|$ could be most reasonably interpreted as the characteristics of a reversible coupling/decoupling reaction. After the photocatalytic coupling reaction proceeded to a certain point, an equilibrium between the coupling and decoupling was established, reaching a nonunity $\theta_{t=\infty}$. In this case, the k obtained from the kinetic results represented the sum of the forward and reverse rate constants, while $\theta_{t=\infty}$ was determined by the ratio between forward and reverse reaction rates. Increasing the excitation power would accelerate the coupling reaction without changing the decoupling reaction rates, thereby shifting the equilibrium toward the DMAB and resulting in increased $\theta_{t=\infty}$. However, after the 4-ATP molecules were photocatalytically converted into DMAB on SiO_2@Ag NC SNPs, no reverse reaction was observed even without laser illumination. As shown in Figure S7 in the Supporting Information, $\theta_{t=\infty}$ reached ∼0.95 after illuminating 4-ATP-coated SNPs with the 785 nm laser at 0.56

DOI: 10.1021/acs.jpcc.8b00660
J. Phys. Chem. C 2018, 122, 5686−5697

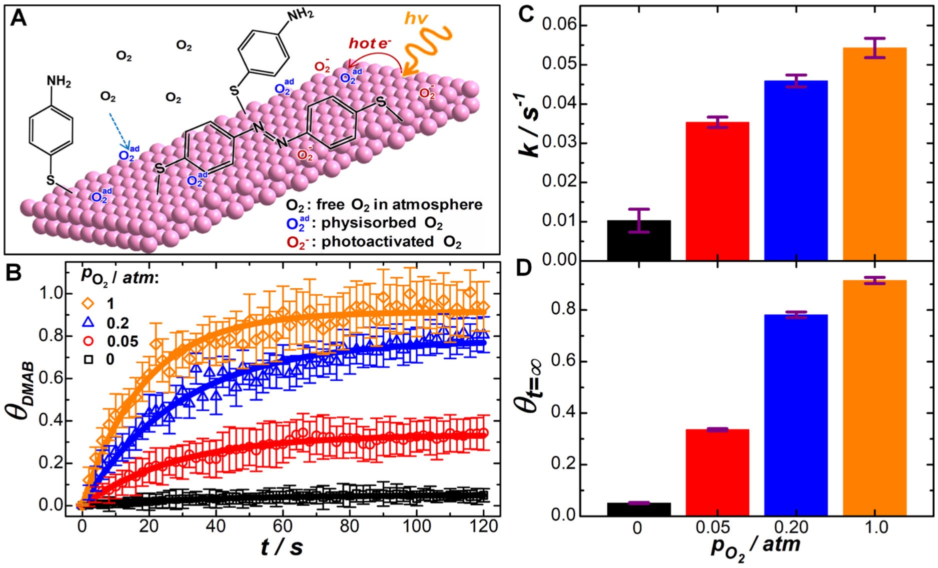

Figure 3. Effects of interfacial oxygen abundance on photocatalytic coupling of 4-ATP. (A) Schematic illustration of the coexistence of three oxygen species: free O_2 in the atmosphere, O_2 adsorbed on Ag surfaces (O_2^{ad}), and photoactivated O_2 (O_2^-). (B) θ_{DMAB} as a function of reaction time, t, under laser illumination (785 nm, 0.45 mW) at various p_{O_2}. The spectral acquisition time for each time-resolved SERS spectra was 2 s. The θ_{DMAB} trajectories show the averaged results collected on 10 different SiO$_2$@Ag NC SNPs under each experimental condition, and the error bars represent the standard deviations. The results of least-squares fitting are shown as solid curves in panel (B). (C) k and (D) $\theta_{t=\infty}$ at various p_{O_2}. The error bars show the standard deviations of least-squares curve fitting.

mM for ~50 s and no apparent decrease of $\theta_{t=\infty}$ was observed after decreasing the laser power to 0.32 mM. These observations strongly indicated that the photocatalytic coupling of 4-ATP could be considered as an irreversible reaction under the current conditions. The reverse reaction, decoupling of DMAB, was so slow that it became unobservable within the experimentally measured time scales. We hypothesized that the partial conversion of 4-ATP to DMAB at low excitation powers was due to the presence of a subpopulation of surface-adsorbed 4-ATP that remained unreactive. This unreactive subpopulation, however, may be thermally activated by photothermal annealing, following the plamsonic excitations, which well-explained why $\theta_{t=\infty}$ increased with both the optical field, $|E|$, of the photocatalysts and the excitation power. The effects of the photothermal annealing will be discussed in greater detail later in this paper.

As shown by eq 9, k could also be modulated by varying the abundance of surface-adsorbed oxygen, $[O_2^{ad}]$, without changing k_1, k_{-1}, and k_2, which could be experimentally realized by adjusting the partial pressure of O_2, p_{O_2}, in the reaction atmosphere. As illustrated in Figure 3A, only when the molecular O_2 was physisorbed on the Ag surfaces could the plasmonic hot electrons be transferred from Ag to O_2 to generate photoactivated oxygen. $[O_2^-]_{ss}$ is directly proportional to $[O_2^{ad}]$, which was controlled by p_{O_2}. To control p_{O_2} in the reaction atmosphere, we co-flowed O_2 and N_2 into the reaction chamber with controlled relative flow rates while keeping the total pressure at 1 atm, using a flow cell with an inlet and an outlet similar to the ones we previously used for single-molecule fluorescence measurements,[53] except that the flow cell was assembled on a silicon substrate instead of a polyethylene glycol-functionalized glass coverslip. As shown in Figure 3B,C, k increased with p_{O_2}, further verifying the reaction mechanism we proposed. Although kinetically very slow, the photocatalytic oxidative coupling of 4-ATP still took place with a small but nonzero k even in pure N_2 atmosphere ($p_{O_2} = 0$), mostly likely driven by plasmonic hot holes. As illustrated in Figure 2A, the highest occupied molecular orbital (HOMO) of 4-ATP chemisorbed on Ag was calculated to be −5.5 eV versus vacuum, 1.2 eV below the Ag Fermi level.[48,49] In principle, it is also possible to use an electron in the HOMO of chemisorbed 4-ATP to fill a hot hole in Ag following plasmonic excitation at 785 nm. However, the plasmonic hot hole-driven oxidative coupling of 4-ATP was kinetically much slower than its hot electron-driven counterpart under the aerobatic conditions because of the low abundance of hot holes below −5.5 eV versus vacuum. At 785 nm, we essentially excited the plasmonic intraband transitions, which preferentially favored the generation of energetic hot electrons exploitable for photocatalytic reactions, while efficient generation of energetic hot holes requires excitation of the interband transitions of Ag at wavelengths shorter than 330 nm.[15] As shown in Figure 3B,D, $\theta_{t=\infty}$ also increased with p_{O_2}, suggesting that an O_2-rich atmosphere was favorable to the thermal activation of surface-adsorbed molecular 4-ATP. We hypothesized that a strong synergy existed between the photoactivation of surface-adsorbed oxygen and the photothermal activation of chemisorbed 4-ATP, though the detailed mechanisms still remained open to further scrutiny.

While both k_1 and $[O_2^{ad}]$ were the key factors determining $[O_2^-]_{ss}$, k_2 was intimately related to the molecular structures and interfacial behaviors of the thiophenol derivatives chemisorbed on Ag surfaces. In the context of our proposed kinetic model, k_2 was determined by the activation energy barrier of the rate-limiting step, which was associated with the dissociation of the N−H bonds in the amine group of 4-ATP. Therefore, when substituting the amine group of 4-ATP with a dimetheylamine group (4-DMATP) or a acetylamine group (4-AATP), k_2 changed significantly because it was tied to the nature and strength of the chemical bonds on the N atom. The

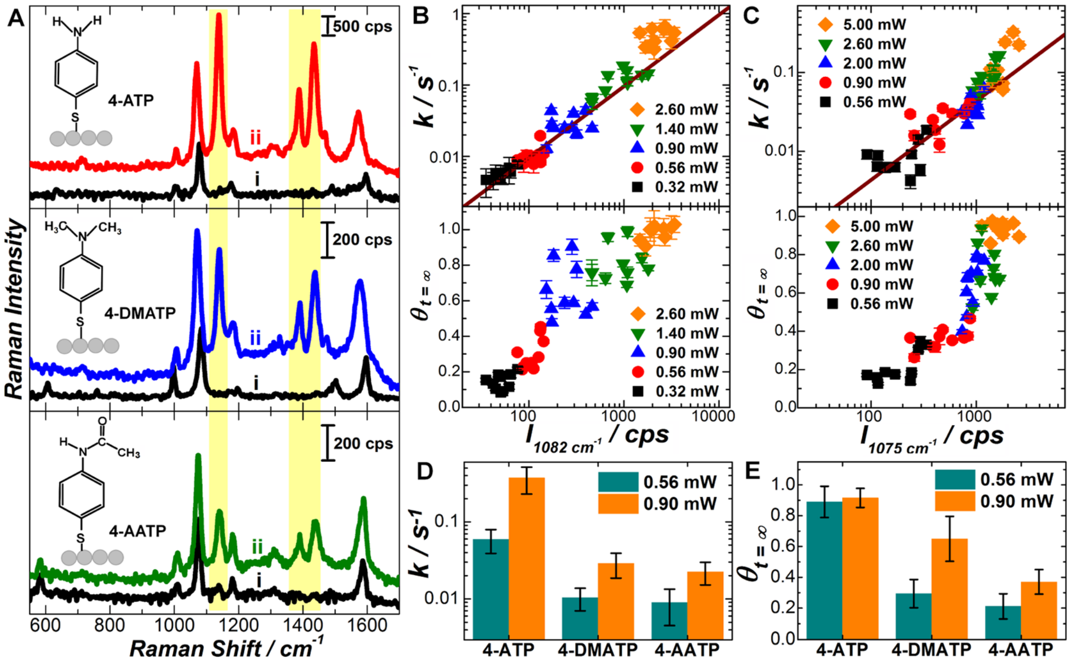

Figure 4. Molecular structural effects on photocatalytic coupling of thiophenol derivatives. (A) Representative SERS spectra of 4-ATP, 4-DMATP, and 4-AATP (i) before and (ii) after the oxidative coupling reaction under laser illumination (785 nm, 0.90 mW) for 120 s. The spectra acquisition time was 1 s for 4-ATP and 2 s for 4-DMATP and 4-AATP. (B) Plots of k (upper panel) and $\theta_{t=\infty}$ (lower panel) vs the initial SERS intensities at 1082 cm^{-1}, $I_{1082\mathrm{cm}^{-1}}$, collected on individual 4-DMATP-coated SiO$_2$@Ag NC SNPs at excitation powers of 0.32, 0.56, 0.90, 1.40, and 2.60 mW. (C) Plots of k (upper panel) and $\theta_{t=\infty}$ (lower panel) vs the initial SERS intensities at 1075 cm^{-1}, $I_{1075\mathrm{cm}^{-1}}$, collected on individual 4-AATP-coated SiO$_2$@Ag NC SNPs at excitation powers of 0.56, 0.90, 2.00, 2.60, and 5.00 mW. The time-resolved SERS measurements were performed on 10 different SiO$_2$@Ag NC SNPs at each excitation power, and the error bars represented the standard deviations of least-squares curve fitting. Comparison of (D) k and (E) $\theta_{t=\infty}$ of 4-ATP, 4-DMATP, and 4-AATP at excitation powers of 0.56 and 0.90 mW. The error bars represented the standard deviations of 10 SiO$_2$@Ag NC SNPs under each condition.

SERS and normal Raman spectra of 4-ATP, 4-DMATP, and 4-AATP are shown in Figure S8, and the assignments of the major SERS peaks are listed in Tables S1, S3, and S4 in the Supporting Information. As shown in Figure 4A, all the three thiophenol derivatives, when chemisorbed on the SiO$_2$@Ag NC SNPs, underwent plasmon-driven oxidative coupling processes to form DMAB upon exposure to 785 nm laser at an excitation power of 0.90 mW. Analogous to that of 4-ATP, the photocatalytic coupling reactions of both 4-DMATP and 4-AATP also obeyed the first-order rate law (Figures S9 and S10 in the Supporting Information). The first-order rate constants of both the 4-DMATP and 4-AATP coupling reactions were observed to be proportional to initial SERS intensity of the C−S stretching modes (1082 cm^{-1} for 4-DMATP and 1075 cm^{-1} for 4-AATP) in low excitation power regimes and switched to a superlinear power-law dependence at higher excitation powers (upper panels in Figure 4B,C). Similar to that of 4-ATP coupling, the $\theta_{t=\infty}$ for the 4-DMATP and 4-AATP coupling reactions also increased with initial SERS intensity of the C−S stretching modes, approaching 100% apparent reaction yields at sufficiently high excitation powers (lower panels in Figure 4B,C). These results strongly indicated that the proposed mechanism for the photocatalytic oxidative coupling of 4-ATP, which involved the steady-state photoactivated oxygen, could be used as a generic kinetic model to interpret the kinetics of 4-DMATP and 4-AATP coupling reactions as well. However, both k and $\theta_{t=\infty}$ varied significantly under the same experimental conditions (the same excitation power and p_{O_2}) when the molecular structures of the thiophenol derivatives changed. As shown in Figure 4D,E, both k and $\theta_{t=\infty}$ followed the same trend of 4-ATP > 4-DMATP > 4-AATP.

The different k values among the three thiophenol derivatives essentially stemmed from the difference in k_2, which was related to the polarities and dissociation energies of the chemical bonds. k_2 for 4-ATP was significantly higher than that for 4-DMATP under the same experimental conditions because the N−H bond in 4-ATP was remarkably more polar and thus easier to dissociate than the N−C bond in 4-DMATP when reacting with the photoactivated oxygen. In addition, 4-ATP exhibited smaller steric hindrance than 4-DMATP for the photoactivated oxygen to attack the leaving groups, which were H atoms for 4-ATP and methyl groups for 4-DMATP. Among the three thiophenol derivatives, 4-AATP exhibited the smallest k and lowest $\theta_{t=\infty}$ because the N−C bond in 4-AATP was partially double-bonded in nature as a consequence of electron delocalization in the acetylamine group, thereby creating a markedly higher energy barrier for the bond dissociation.

k_2 was found to be related to not only the intrinsic molecular structures but the photothermal heating of the surface-adsorbed thiophenol derivatives as well. Following the optical excitation of plasmon resonances, the energetic hot electrons may also undergo thermal dissipation to heat up the metal lattices via electron−phonon coupling.[10] At relatively low excitation power, the photothermal heating of the interfacial molecular adsorbates had insignificant impact to the overall reaction kinetics. Therefore, k was observed to be proportional to $|E|^4$ of the photocatalysts for all 4-ATP (Figure 2F), 4-DMATP (Figure 4B), and 4-AATP (Figure 4C). Above a certain threshold excitation power, however, a superlinear power-law

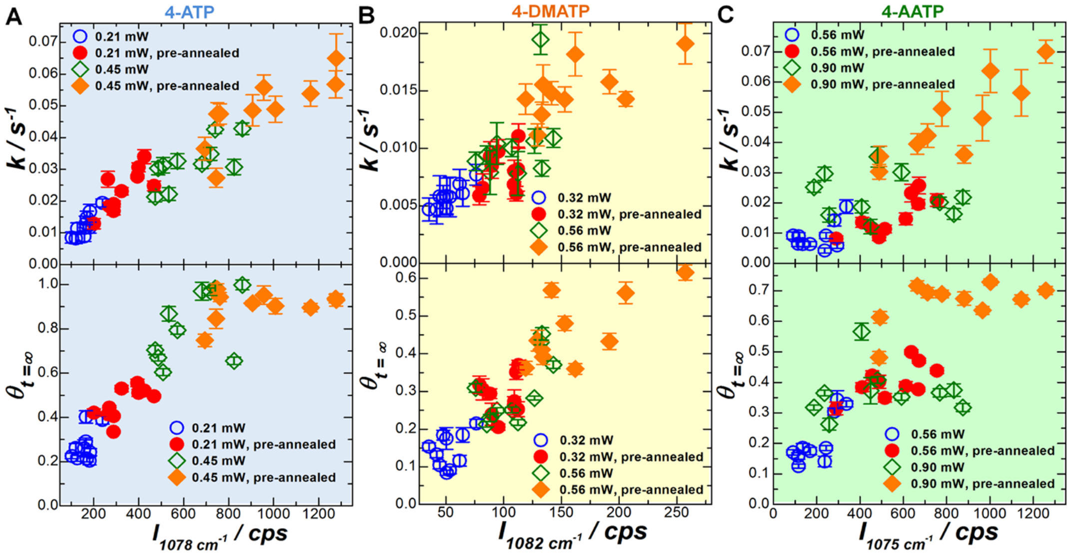

Figure 5. Thermal effects on photocatalytic coupling of thiophenol derivatives. Plots of k (top panels) and $\theta_{t=\infty}$ (bottom panels) vs the initial SERS intensities of the C−S stretching modes of (A) 4-ATP, (B) 4-DMATP, and (C) 4-AATP. The kinetic results obtained on preannealed samples and those without preannealing treatments were compared under various excitation laser intensities. Under each condition, the time-resolved SERS measurements were performed on 10 different SiO_2@Ag NC SNPs, and the error bars represented the standard deviations of least-squares curve fitting.

dependence of k on the $|E|^4$ of the photocatalysts was observed because of increased local reaction temperatures and thermally induced restructuring of the molecular adsorbates, both of which led to the decrease of reaction energy barriers and thus increased k_2. In Figure S11 in the Supporting Information, we compared the SERS spectra of 4-ATP, 4-DMATP, and 4-AATP before and after laser illumination for 60 s in the presence of pure N_2. While almost no DMAB formation was observed within 60 s in such a O_2-free environment, a significant increase in the SERS peak intensities was clearly observed on all the three thiophenol derivatives, which could be interpreted as a consequence of photothermally induced strengthening of the interactions between the adsorbate molecules and Ag NC surfaces. We also observed that the SERS intensities of 4-ATP increased by about 100% upon thermal annealing at 90 °C for 1 h prior to SERS measurements (Figure S12 in the Supporting Information). The additional SERS enhancements upon thermal annealing was also previously observed by Aggarwal and co-workers on the benzenethiol adsorbed on nanostructured Ag films, which was interpreted as a consequence of thermally induced transitions between various adsorption states of benzenethiol.[54]

To further verify the photothermal effects on the reaction rate, we measured the kinetics of the photocatalytic coupling of 4-ATP with time intervals of 60 s inserted between successive SERS spectral acquisitions instead of continuous illumination (Figure S13 in the Supporting Information). Adding the time intervals allowed the photothermally generated heat to dissipate to the environment before the next cycle of laser excitation started such that the local heating at the molecule−nanoparticle interfaces could be minimized. Interestingly, switching from continuous to discontinuous illuminations did not result in much difference in k and $I_{1078\mathrm{cm}^{-1}}$ at excitation power of 0.45 mW, suggesting that the photothermal effect was insignificant at this excitation power, which is in agreement with the results shown in Figure 2F. However, an obvious decrease in both k and $I_{1078\mathrm{cm}^{-1}}$ was observed when the time intervals were included during the kinetic measurements at the excitation power of 0.90 mW, which was in a power regime where k exhibited a superlinear power-law dependence on $|E|^4$ because of significant photothermal effects.

The plasmonic photothermal annealing of the surface-adsorbed thiophenol derivatives also greatly influenced $\theta_{t=\infty}$. In the low excitation power regime, only a fraction of 4-ATP molecules, most likely the ones experiencing the strongest fields in the interstitial plasmonic hot spots, could be photothermally activated and subsequently transformed into DMAB, while those in the plasmonic "colder" region remained unreactive because of insufficient photothermal heating. Takeyasu and co-authors recently discovered that only when the excitation laser power was above a threshold value could the photocatalytic coupling of 4-ATP occur,[55] though the underlying mechanisms were not further discussed. Although the hot spots provided the locations for the strongest SERS enhancements, the unreactive 4-ATP in the plasmonic "colder" regions also contributed to the overall SERS signals. As the excitation power increased, increasing fractions of the molecules started to be located in regions with local fields sufficiently high for the thermal activation, resulting in increased $\theta_{t=\infty}$ until $\theta_{t=\infty}$ approached 1 at sufficiently high excitation powers, nominally 0.56 mW for 4-ATP, 1.40 mW for 4-DMATP, and 2.60 mW for 4-AATP, under the current experimental conditions.

The thermal effects on the kinetics and yields of the photocatalytic oxidative coupling of 4-ATP, 4-DMATP, and 4-AATP were further verified by preannealing the samples at 90 °C for 1 h to optimize the structures and thus thermally activate the surface-adsorbed thiophenol derivatives prior to the time-resolved SERS measurements. In Figure 5, we showed the correlations of k and $\theta_{t=\infty}$ with the initial SERS intensities of the C−S stretching modes of the reactants for both preannealed and unannealed samples. The preannealing of the samples gave rise to further enhanced SERS signals while the positions and the line shapes of all the characteristic SERS peaks were well-preserved, verifying that the thermal treatments of the samples neither induced any thermal coupling reactions nor caused any sample damage. The preannealing treatments resulted in a significant increase of both k and $\theta_{t=\infty}$ for all the three thiophenol derivatives we investigated in comparison to those of the unannealed samples, and this generic trend held true when varying the excitation power. The results shown in Figure 5 provided important insights into the underlying thermal effects on the kinetics and yields of the photocatalytic oxidative coupling of thiophenol derivatives, which well-interpreted the superlinear power-law dependence of k and $\theta_{t=\infty}$ on the local fields of the photocatalysts observed at high excitation powers.

■ CONCLUSIONS

We have resolved the complex kinetics of photocatalytic oxidative coupling of thiophenol derivatives chemisorbed on the surfaces of optically excited plasmonic photocatalysts using time-resolved SERS as a plasmon-enhanced spectroscopic tool. This work provides quantitative mechanistic insights on a series of fundamentally important issues that have long been poorly understood. First, the rate-limiting steps have been identified to be associated with the thermal reactions between photo-activated oxygen and surface-adsorbed thiophenol derivatives rather than the plasmon-driven photoactivation of interfacial oxygen. Second, photoactivation of interfacial oxygen occurs upon transfer of a hot electron from Ag to the physisorbed oxygen through Landau damping. When the photoactivation of oxygen is much faster than the rate-limiting step, the rates of the coupling reactions are dynamically maneuvered by the photoactivated oxygen at its steady-state concentrations, giving rise to an apparent first-order overall reaction kinetics. The steady-state concentration of photoactivated oxygen can be experimentally tuned by selectively varying the excitation power, the local optical fields, and the abundance of interfacial oxygen. Third, time-resolved SERS measurements allow us to quantitatively correlate the reaction rates with the local field intensities on the surfaces of the photocatalysts. The rate constants switch from a linear dependence to a superlinear power-law dependence with respect to the fourth power of the local fields as the excitation power progressively increases, essentially because of the plasmonic photothermal effects. Fourth, the rate constants of the rate-limiting steps are related to the molecular structures and thermal restructuring of the thiophenol derivatives chemisorbed on the nanoparticle surfaces. The plasmonic photothermal heating of the surface adsorbates may not only modify the molecular adsorption states but also thermally activate the thiophenol derivatives for the subsequent oxidative coupling reactions, significantly enhancing both the rates and the yields of the reactions.

The knowledge gained from this work provides key design principles guiding the rational optimization of plasmon-driven photocatalytic processes. The photoactivated oxygen has been found to be a crucial transient species broadly involved in a variety of photocatalytic oxidation reactions.[11,14,30−34] Therefore, the insights gained from the time-resolved SERS measurements may serve as a generic central knowledge framework that guides us to rationally maneuver the kinetics of a wide range of oxidation reactions driven by energetic hot electrons. Analogous to oxygen, interfacial molecular hydrogen can also be photoactivated when interacting with optically excited plasmonic nanostructures.[23,24] We believe that the plasmonically activated hydrogen species may be harnessed to drive photocatalytic reductive chemical transformations as well. The kinetic model involving the steady-state photoactivated species proposed in this work provides important implications that may broadly apply to a large variety of plasmon-driven photocatalytic reactions, greatly enhancing our capabilities to selectively and efficiently drive unconventional photocatalytic chemical transformations by fine-tailoring the plasmonic characteristics of the photocatalysts and the interfacial molecule−nanoparticle interactions.

■ ASSOCIATED CONTENT

Ⓢ Supporting Information

The Supporting Information is available free of charge on the ACS Publications website at DOI: 10.1021/acs.jpcc.8b00660.

> Experimental details, tables listing Raman peak assignments and figures including SEM images, TEM images, dark-field scattering images, ζ-potential results, and time-resolved SERS results as noted in the text (PDF)

■ AUTHOR INFORMATION

Corresponding Author

*E-mail: wang344@mailbox.sc.edu. Phone: 803-777-2203. Fax: 803-777-9521.

ORCID

Hui Wang: 0000-0002-1874-5137

Notes

The authors declare no competing financial interest.

■ ACKNOWLEDGMENTS

This work was supported by a seed grant provided by the University of South Carolina (USC) Office of Vice President for Research through an ASPIRE-I Track-I Award and in part by National Science Foundation through a CAREER Award (DMR-1253231) and an EPSCoR RII Track-I Award (OIA-1655740). Q.Z. was partially supported by a Dissertation Fellowship from USC NanoCenter and a SPARC Graduate Research Award from the USC Office of the Vice President for Research. This work made use of the facilities at the USC Electron Microscopy Center and W. M. Keck Open Laboratory.

■ REFERENCES

(1) Schuller, J. A.; Barnard, E. S.; Cai, W.; Jun, Y. C.; White, J. S.; Brongersma, M. L. Plasmonics for Extreme Light Concentration and Manipulation. *Nat. Mater.* **2010**, *9*, 193−204.

(2) Kauranen, M.; Zayats, A. V. Nonlinear Plasmonics. *Nat. Photonics* **2012**, *6*, 737−748.

(3) Ciraci, C.; Hill, R. T.; Mock, J. J.; Urzhumov, Y.; Fernandez-Dominguez, A. I.; Maier, S. A.; Pendry, J. B.; Chilkoti, A.; Smith, D. R. Probing the Ultimate Limits of Plasmonic Enhancement. *Science* **2012**, *337*, 1072−1074.

(4) Fang, Y.; Seong, N.-H.; Dlott, D. D. Measurement of the Distribution of Site Enhancements in Surface-Enhanced Raman Scattering. *Science* **2008**, *321*, 388−392.

(5) Knight, M. W.; Sobhani, H.; Nordlander, P.; Halas, N. J. Photodetection with Active Optical Antennas. *Science* **2011**, *332*, 702−704.

(6) Wu, K.; Chen, J.; McBride, J. R.; Lian, T. Efficient Hot-Electron Transfer by a Plasmon-Induced Interfacial Charge-Transfer Transition. *Science* **2015**, *349*, 632−635.

(7) Clavero, C. Plasmon-Induced Hot-Electron Generation at Nanoparticle/Metal-Oxide Interfaces for Photovoltaic and Photocatalytic Devices. *Nat. Photonics* **2014**, *8*, 95−103.

(8) Manjavacas, A.; Liu, J. G.; Kulkarni, V.; Nordlander, P. Plasmon-Induced Hot Carriers in Metallic Nanoparticles. *ACS Nano* **2014**, *8*, 7630−7638.

(9) Govorov, A. O.; Zhang, H.; Gun'ko, Y. K. Theory of Photoinjection of Hot Plasmonic Carriers from Metal Nanostructures

into Semiconductors and Surface Molecules. *J. Phys. Chem. C* **2013**, *117*, 16616−16631.

(10) Brongersma, M. L.; Halas, N. J.; Nordlander, P. Plasmon-Induced Hot Carrier Science and Technology. *Nat. Nanotechnol.* **2015**, *10*, 25−34.

(11) Christopher, P.; Xin, H.; Marimuthu, A.; Linic, S. Singular Characteristics and Unique Chemical Bond Activation Mechanisms of Photocatalytic Reactions on Plasmonic Nanostructures. *Nat. Mater.* **2012**, *11*, 1044−1050.

(12) Mubeen, S.; Lee, J.; Singh, N.; Krämer, S.; Stucky, G. D.; Moskovits, M. An Autonomous Photosynthetic Device in Which All Charge Carriers Derive from Surface Plasmons. *Nat. Nanotechnol.* **2013**, *8*, 247−251.

(13) Linic, S.; Aslam, U.; Boerigter, C.; Morabito, M. Photochemical Transformations on Plasmonic Metal Nanoparticles. *Nat. Mater.* **2015**, *14*, 567−576.

(14) Linic, S.; Christopher, P.; Ingram, D. B. Plasmonic Metal Nanostructures for Efficient Conversion of Solar to Chemical Energy. *Nat. Mater.* **2011**, *10*, 911−921.

(15) Govorov, A. O.; Zhang, H.; Demir, H. V.; Gun'ko, Y. K. Photogeneration of Hot Plasmonic Electrons with Metal Nanocrystals: Quantum Description and Potential Applications. *Nano Today* **2014**, *9*, 85−101.

(16) Brus, L. Noble Metal Nanocrystals: Plasmon Electron Transfer Photochemistry and Single-Molecule Raman Spectroscopy. *Acc. Chem. Res.* **2008**, *41*, 1742−1749.

(17) Jin, R.; Cao, Y.; Mirkin, C. A.; Kelly, K. L.; Schatz, G. C.; Zheng, J. G. Photoinduced Conversion of Silver Nanospheres to Nanoprisms. *Science* **2001**, *294*, 1901−1903.

(18) Jin, R.; Cao, Y. C.; Hao, E.; Métraux, G. S.; Schatz, G. C.; Mirkin, C. A. Controlling Anisotropic Nanoparticle Growth through Plasmon Excitation. *Nature* **2003**, *425*, 487−490.

(19) Marimuthu, A.; Zhang, J.; Linic, S. Tuning Selectivity in Propylene Epoxidation by Plasmon Mediated Photo-Switching of Cu Oxidation State. *Science* **2013**, *339*, 1590−1593.

(20) Zhai, Y.; DuChene, J. S.; Wang, Y.-C.; Qiu, J.; Johnston-Peck, A. C.; You, B.; Guo, W.; DiCiaccio, B.; Qian, K.; Zhao, E. W.; et al. Polyvinylpyrrolidone-Induced Anisotropic Growth of Gold Nanoprisms in Plasmon-Driven Synthesis. *Nat. Mater.* **2016**, *15*, 889−895.

(21) Deeb, C.; Ecoffet, C.; Bachelot, R.; Plain, J.; Bouhelier, A.; Soppera, O. Plasmon-Based Free-Radical Photopolymerization: Effect of Diffusion on Nanolithography Processes. *J. Am. Chem. Soc.* **2011**, *133*, 10535−10542.

(22) Ueno, K.; Juodkazis, S.; Shibuya, T.; Yokota, Y.; Mizeikis, V.; Sasaki, K.; Misawa, H. Nanoparticle Plasmon-Assisted Two-Photon Polymerization Induced by Incoherent Excitation Source. *J. Am. Chem. Soc.* **2008**, *130*, 6928−6929.

(23) Mukherjee, S.; Libisch, F.; Large, N.; Neumann, O.; Brown, L. V.; Cheng, J.; Lassiter, J. B.; Carter, E. A.; Nordlander, P.; Halas, N. J. Hot Electrons Do the Impossible: Plasmon-Induced Dissociation of H_2 on Au. *Nano Lett.* **2013**, *13*, 240−247.

(24) Mukherjee, S.; Zhou, L.; Goodman, A. M.; Large, N.; Ayala-Orozco, C.; Zhang, Y.; Nordlander, P.; Halas, N. J. Hot-Electron-Induced Dissociation of H_2 on Gold Nanoparticles Supported on SiO_2. *J. Am. Chem. Soc.* **2014**, *136*, 64−67.

(25) Lee, J.; Mubeen, S.; Ji, X.; Stucky, G. D.; Moskovits, M. Plasmonic Photoanodes for Solar Water Splitting with Visible Light. *Nano Lett.* **2012**, *12*, 5014−5019.

(26) Xie, W.; Schlücker, S. Hot Electron-Induced Reduction of Small Molecules on Photorecycling Metal Surfaces. *Nat. Commun.* **2015**, *6*, 7570.

(27) Brandt, N. C.; Keller, E. L.; Frontiera, R. R. Ultrafast Surface-Enhanced Raman Probing of the Role of Hot Electrons in Plasmon-Driven Chemistry. *J. Phys. Chem. Lett.* **2016**, *7*, 3179−3185.

(28) Sun, M.; Xu, H. A Novel Application of Plasmonics: Plasmon-Driven Surface-Catalyzed Reactions. *Small* **2012**, *8*, 2777−2786.

(29) van Schrojenstein Lantman, E. M.; Deckert-Gaudig, T.; Mank, A. J. G.; Deckert, V.; Weckhuysen, B. M. Catalytic Processes Monitored at the Nanoscale with Tip-Enhanced Raman Spectroscopy. *Nat. Nanotechnol.* **2012**, *7*, 583−586.

(30) Christopher, P.; Xin, H.; Linic, S. Visible-Light-Enhanced Catalytic Oxidation Reactions on Plasmonic Silver Nanostructures. *Nat. Chem.* **2011**, *3*, 467−472.

(31) Kale, M. J.; Avanesian, T.; Christopher, P. Direct Photocatalysis by Plasmonic Nanostructures. *ACS Catal.* **2014**, *4*, 116−128.

(32) Fang, Y.; Li, Y.; Xu, H.; Sun, M. Ascertaining p,p′-Dimercaptoazobenzene Produced from p-Aminothiophenol by Selective Catalytic Coupling Reaction on Silver Nanoparticles. *Langmuir* **2010**, *26*, 7737−7746.

(33) Huang, Y.-F.; Zhu, H.-P.; Liu, G.-K.; Wu, D.-Y.; Ren, B.; Tian, Z.-Q. When the Signal Is Not from the Original Molecule To Be Detected: Chemical Transformation of para-Aminothiophenol on Ag during the SERS Measurement. *J. Am. Chem. Soc.* **2010**, *132*, 9244−9246.

(34) Linic, S.; Christopher, P.; Xin, H.; Marimuthu, A. Catalytic and Photocatalytic Transformations on Metal Nanoparticles with Targeted Geometric and Plasmonic Properties. *Acc. Chem. Res.* **2013**, *46*, 1890−1899.

(35) Wang, F.; Li, C.; Chen, H.; Jiang, R.; Sun, L.-D.; Li, Q.; Wang, J.; Yu, J. C.; Yan, C.-H. Plasmonic Harvesting of Light Energy for Suzuki Coupling Reactions. *J. Am. Chem. Soc.* **2013**, *135*, 5588−5601.

(36) Sarina, S.; Zhu, H.; Jaatinen, E.; Xiao, Q.; Liu, H.; Jia, J.; Chen, C.; Zhao, J. Enhancing Catalytic Performance of Palladium in Gold and Palladium Alloy Nanoparticles for Organic Synthesis Reactions through Visible Light Irradiation at Ambient Temperatures. *J. Am. Chem. Soc.* **2013**, *135*, 5793−5801.

(37) Guo, J.; Zhang, Y.; Shi, L.; Zhu, Y.; Mideksa, M. F.; Hou, K.; Zhao, W.; Wang, D.; Zhao, M.; Zhang, X.; et al. Boosting Hot Electrons in Hetero-Superstructures for Plasmon-Enhanced Catalysis. *J. Am. Chem. Soc.* **2017**, *139*, 17964−17972.

(38) Huang, Y.-F.; Zhang, M.; Zhao, L.-B.; Feng, J.-M.; Wu, D.-Y.; Ren, B.; Tian, Z.-Q. Activation of Oxygen on Gold and Silver Nanoparticles Assisted by Surface Plasmon Resonances. *Angew. Chem., Int. Ed.* **2014**, *53*, 2353−2357.

(39) Osawa, M.; Matsuda, N.; Yoshii, K.; Uchida, I. Charge-Transfer Resonance Raman Process in Surface-Enhanced Raman-Scattering from P-Aminothiophenol Adsorbed on Silver - Herzberg-Teller Contribution. *J. Phys. Chem.* **1994**, *98*, 12702−12707.

(40) Xu, P.; Kang, L.; Mack, N. H.; Schanze, K. S.; Han, X.; Wang, H.-L. Mechanistic Understanding of Surface Plasmon Assisted Catalysis on a Single Particle: Cyclic Redox of 4-Aminothiophenol. *Sci. Rep.* **2013**, *3*, 2997.

(41) Dai, Z. G.; Xiao, X. H.; Wu, W.; Zhang, Y. P.; Liao, L.; Guo, S. S.; Ying, J. J.; Shan, C. X.; Sun, M. T.; Jiang, C. Z. Plasmon-Driven Reaction Controlled by the Number of Graphene Layers and Localized Surface Plasmon Distribution during Optical Excitation. *Light: Sci. Appl.* **2015**, *4*, No. e342.

(42) Sun, M.; Huang, Y.; Xia, L.; Chen, X.; Xu, H. The pH-Controlled Plasmon-Assisted Surface Photocatalysis Reaction of 4-Aminothiophenol to p,p′-Dimercaptoazobenzene on Au, Ag, and Cu Colloids. *J. Phys. Chem. C* **2011**, *115*, 9629−9636.

(43) Zheng, T.; Zhang, Q.; Feng, S.; Zhu, J.-J.; Wang, Q.; Wang, H. Robust Nonenzymatic Hybrid Nanoelectrocatalysts for Signal Amplification toward Ultrasensitive Electrochemical Cytosensing. *J. Am. Chem. Soc.* **2014**, *136*, 2288−2291.

(44) Wang, H.; Halas, N. J. Mesoscopic Au "Meatball" particles. *Adv. Mater.* **2008**, *20*, 820−825.

(45) Xia, X.; Zeng, J.; Oetjen, L. K.; Li, Q.; Xia, Y. Quantitative Analysis of the Role Played by Poly(vinylpyrrolidone) in Seed-Mediated Growth of Ag Nanocrystals. *J. Am. Chem. Soc.* **2012**, *134*, 1793−1801.

(46) Halas, N. J.; Lal, S.; Chang, W.-S.; Link, S.; Nordlander, P. Plasmons in Strongly Coupled Metallic Nanostructures. *Chem. Rev.* **2011**, *111*, 3913−3961.

(47) Malynych, S.; Luzinov, I.; Chumanov, G. Poly(vinyl pyridine) as a Universal Surface Modifier for Immobilization of Nanoparticles. *J. Phys. Chem. B* **2002**, *106*, 1280−1285.

(48) Zhao, L.-B.; Liu, X.-X.; Zhang, M.; Liu, Z.-F.; Wu, D.-Y.; Tian, Z.-Q. Surface Plasmon Catalytic Aerobic Oxidation of Aromatic Amines in Metal/Molecule/Metal Junctions. *J. Phys. Chem. C* **2016**, *120*, 944−955.

(49) Zhao, L.-B.; Zhang, M.; Huang, Y.-F.; Williams, C. T.; Wu, D.-Y.; Ren, B.; Tian, Z.-Q. Theoretical Study of Plasmon-Enhanced Surface Catalytic Coupling Reactions of Aromatic Amines and Nitro Compounds. *J. Phys. Chem. Lett.* **2014**, *5*, 1259−1266.

(50) Campion, A.; Kambhampati, P. Surface-enhanced Raman scattering. *Chem. Soc. Rev.* **1998**, *27*, 241−250.

(51) Willets, K. A.; Van Duyne, R. P. Localized Surface Plasmon Resonance Spectroscopy and Sensing. *Annu. Rev. Phys. Chem.* **2007**, *58*, 267−297.

(52) Li, J. F.; Huang, Y. F.; Ding, Y.; Yang, Z. L.; Li, S. B.; Zhou, X. S.; Fan, F. R.; Zhang, W.; Zhou, Z. Y.; Wu, D. Y.; et al. Shell-Isolated Nanoparticle-Enhanced Raman Spectroscopy. *Nature* **2010**, *464*, 392−395.

(53) Wang, H.; Musier-Forsyth, K.; Falk, C.; Barbara, P. F. Single-Molecule Spectroscopic Study of Dynamic Nanoscale DNA Bending Behavior of HIV-1 Nucleocapsid Protein. *J. Phys. Chem. B* **2013**, *117*, 4183−4196.

(54) Aggarwal, R. L.; Farrar, L. W.; Saikin, S. K. Increase of SERS Signal upon Heating or Exposure to a High-Intensity Laser Field: Benzenethiol on an AgFON Substrate. *J. Phys. Chem. C* **2012**, *116*, 16656−16659.

(55) Takeyasu, N.; Kagawa, R.; Sakata, K.; Kaneta, T. Laser Power Threshold of Chemical Transformation on Highly Uniform Plasmonic and Catalytic Nanosurface. *J. Phys. Chem. C* **2016**, *120*, 12163−12169.